

Interfacial Strain Effects on Lithium Diffusion Pathways in the Spinel Solid Electrolyte Li-Doped MgAl_2O_4

Conn O'Rourke* and Benjamin J. Morgan†

Department of Chemistry, University of Bath, Bath, BA2 7AX

(Dated: December 14, 2024)

(Li,Al)-co-doped magnesium spinel ($\text{Li}_x\text{Mg}_{1-2x}\text{Al}_{2+x}\text{O}_4$) is a solid lithium-ion electrolyte with potential use in all-solid-state lithium-ion batteries. The spinel structure means that interfaces with spinel electrodes, such as $\text{Li}_y\text{Mn}_2\text{O}_4$ and $\text{Li}_{4+3z}\text{Ti}_5\text{O}_{12}$, may be *lattice-matched*, with potentially low interfacial resistances. Small lattice parameter differences across a lattice-matched interface are unavoidable, causing a residual epitaxial strain. This strain potentially modifies lithium diffusion across the electrolyte–electrode interface, consequently affecting overall cell performance. Here we report a density functional theory study of strain effects on lithium diffusion pathways for (Li,Al)-co-doped magnesium spinel, for $x_{\text{Li}} = 0.25$ and $x_{\text{Li}} = 0.5$. We have calculated diffusion profiles for the unstrained materials, and for isotropic and biaxial tensile strains of up to 6%, corresponding to $\{100\}$ epitaxial interfaces with $\text{Li}_y\text{Mn}_2\text{O}_4$ and $\text{Li}_{4+3z}\text{Ti}_5\text{O}_{12}$. We find that isotropic tensile strain reduces lithium diffusion barriers from ~ 0.4 eV by as much as 0.28 eV, with typical barriers reduced by ~ 0.15 eV. This effect is associated with increased volumes of transitional octahedral sites, and broadly follows qualitative changes in local electrostatic potentials. For biaxial (epitaxial) strain, which more closely approximates strain at a lattice-matched electrolyte–electrode interface, changes in octahedral site volumes and in lithium diffusion barriers are much smaller than under isotropic strain. These results predict that isotropic strain strongly affects ionic conductivities in (Li,Al)-co-doped magnesium spinel electrolytes, and that tensile strain is a potential route to enhanced lithium transport. For a *lattice-matched* interface with candidate spinel-structured electrodes, however, epitaxial strain has only a small effect on lithium diffusion barriers. From the perspective of local diffusion barriers, therefore, epitaxial strain at coherent lattice-matched electrolyte–electrode interfaces is therefore not expected to strongly affect lithium transport rates or overall cell performance.

INTRODUCTION

Lithium-ion batteries are widely used for energy storage. Historically, the principal applications have been in consumer electronics, but lithium-ion batteries are increasingly finding use in other sectors, such as electric vehicles and grid-scale storage. This success has been tempered by concerns about the stability and safety of the liquid electrolytes found in commercial lithium-ion batteries. Organic liquid electrolytes are flammable, and present an explosion risk if a cell were to short-circuit or suffer mechanical failure. One proposed solution is to replace the liquid electrolytes with electrochemically inert solid lithium-ion conductors. This would eliminate the explosion risk, remove the need for costly protection circuitry, and allow possible battery miniaturization [1–3].

A number of promising lithium-ion solid electrolytes exist; some with ionic conductivities comparable to those of liquid electrolytes [2–4]. For a solid lithium-ion electrolyte to be commercially viable it must be electrically and chemically stable under cell-operating conditions, and have high ionic and negligible electronic conductivities. In an all-solid-state lithium-ion battery, device performance also depends on the interfacial resistance between the electrolyte and electrodes [5]. If a solid electrolyte–electrode pair have crystal structures or lattices that are incommensurate, the electrolyte–electrode interface is expected to be *mismatched*. Lithium-diffusion

pathways across these mismatched interfaces may be highly tortuous, resulting in large interfacial resistances [6].

One strategy for developing all-solid-state batteries with low interfacial resistances is to choose electrolyte–electrode combinations that are *lattice-matched* [6, 7]. If the cathode, electrode, and anode have mutually compatible crystal structures that allow epitaxially coherent interfaces, the diffusion pathways across these solid–solid interfaces are expected to be relatively unobstructed, giving low interfacial resistances. Lattice matching between a solid lithium-ion electrolyte and electrodes was first described by Thackeray and Goodenough in 1985 [7], who suggested using spinel-structured materials for each of the anode, cathode, and electrolyte. Spinel structured electrodes, such as $\text{Li}_y\text{Mn}_2\text{O}_4$ lithium manganese cathodes and $\text{Li}_{4+3z}\text{Ti}_5\text{O}_{12}$ lithium titanate anodes are well known, and are already used in commercial batteries. Spinel-structured electrolytes, however, have long proved elusive. In 2013, Rosciano *et al.* synthesised a new class of spinel-structured lithium-ion electrolytes based on (Li,Al)-co-doped magnesium spinel ($\text{Li}_x\text{Mg}_{1-2x}\text{Al}_{2+x}\text{O}_4$) [6, 8, 9]. This development has revived interest in the possibility of all-solid-state lithium-ion batteries constructed to have a coherent face-centred-cubic (fcc) oxide lattice shared across the anode, electrolyte, and cathode.

Perfect lattice-matching between structurally compatible electrolyte–electrode pairs is not achievable in prac-

system	$a_{\text{expt.}}$ [Å]	Ref.	a_{PBEsol} [Å]
$\text{Li}_y\text{Mn}_2\text{O}_4$	8.144	[10]	
$\text{Li}_{4+3z}\text{Ti}_5\text{O}_{12}$	8.360	[11]	
MgAl_2O_4 ($x_{\text{Li}} = 0$)	8.04	[6]	8.051
$\text{Li}_{0.25}\text{Mg}_{0.5}\text{Al}_{2.25}\text{O}_4$ ($x_{\text{Li}} = 0.25$)	7.96	[6]	7.996
$\text{Li}_{0.5}\text{Al}_{2.5}\text{O}_4$ ($x_{\text{Li}} = 0.5$)	7.89	[6]	7.907

TABLE I. Lattice parameters for lithium manganate and lithium titanate spinels, and for $\text{Li}_x\text{Mg}_{1-2x}\text{Al}_{2+x}\text{O}_4$, from experiment and as calculated (PBEsol) for this work.

tice, and any coherent lattice-matched interface will exhibit some residual strain. For example, the lattice parameter of the parent material MgAl_2O_4 differs from those of LiMn_2O_4 and $\text{Li}_4\text{Ti}_5\text{O}_{12}$ by $\sim 1.3\%$ and 4.0% respectively [10, 11].¹ For (Li,Al)-co-doped MgAl_2O_4 the lattice parameter decreases with increasing lithium concentration (see Table I). The degree of interfacial strain therefore depends not only on the choice of interfacing electrode, but also on the electrolyte stoichiometry.

Residual strain at electrolyte-electrode interfaces may not be without consequences. Lattice strains modify local atomic geometries and distort the potential energy surface that defines lithium diffusion pathways. This affects diffusion barrier heights, and hence ionic conductivities. The effect of interfacial strain on ionic conductivities has been widely studied in fuel cell materials [14–20], motivated by the possibility of straining thin film electrolytes to enhance their oxide-ion conductivities, and hence reduce device operating temperatures. More recently, the concept of “strain engineering” has also been considered as a strategy for enhancing lithium conductivity in lithium-ion electrodes and electrolytes [21–24]. The effect of interfacial strain is particularly pertinent for an electrolyte such as (Li,Al)-co-doped MgAl_2O_4 , where interest is motivated by the possibility of lattice-matching with spinel-structured electrolytes.

Computational modelling provides a powerful tool for studying how factors such as stoichiometry or strain can affect lithium diffusion. To date, the only computational study of lithium transport in (Li,Al)-co-doped magnesium spinel was performed by Mees *et al.* [25]. These authors modelled lithium diffusion at dopant concentrations of $x_{\text{Li}} = 0.125$, $x_{\text{Li}} = 0.25$, and $x_{\text{Li}} = 0.50$, by calculating lithium-ion diffusion barriers using density-functional theory (DFT) nudged-elastic-band (NEB) calculations. These diffusion barriers were then used in kinetic Monte Carlo (kMC) simulations to model long time-scale diffu-

sion. These kMC simulations predicted that increasing x_{Li} from 0.25 to 0.50 causes the lithium diffusion coefficient to increase by $\times 10^2$, with a corresponding decrease in activation energy from 0.61 eV to 0.45 eV.²

Despite this predicted increase in lithium diffusion coefficient with (Li,Al)-dopant concentration, Mees *et al.* suggested that the optimal composition for use with the electrodes $\text{Li}_y\text{Mn}_2\text{O}_4$ or $\text{Li}_{4+3z}\text{Ti}_5\text{O}_{12}$ is $x_{\text{Li}} \approx 0.3$. This effective limit was proposed with two considerations in mind. First, that high lithium content may promote phase separation to poorly conducting LiAl_5O_8 and MgAl_2O_4 . Second, because the bulk lattice parameter of (Li,Al)-co-doped spinel decreases as x_{Li} increases, a higher lithium content corresponds to a *larger* lattice-parameter mismatch with the spinel electrolytes $\text{Li}_y\text{Mn}_2\text{O}_4$ and $\text{Li}_{4+3z}\text{Ti}_5\text{O}_{12}$. This, in turn, was suggested to be likely to increase interfacial resistance, and reduce overall device performance. Subsequent experimental work has shown that (Li,Al)-co-doped spinel can be synthesised at high dopant concentrations (up to $x_{\text{Li}} = 0.4$) without phase separation [9]. The first concern regarding phase stability then, may be (at least partially) avoided through careful synthesis. The second question, however; the effect of epitaxial strain on lithium diffusion, in particular as x_{Li} is increased; remains open.

Here we report density functional theory (DFT) climbing-image nudged-elastic-band (CI-NEB) [26] calculations of lithium diffusion pathways in unstrained, isotropically strained, and epitaxially (biaxially) strained (Li,Al)-co-doped MgAl_2O_4 . We have performed these calculations to better understand the consequences of strain at a hypothetical lattice-matched interface between (Li,Al)-co-doped spinel and the electrodes $\text{Li}_y\text{Mn}_2\text{O}_4$ and $\text{Li}_{4+3z}\text{Ti}_5\text{O}_{12}$. Our calculations assume an implicit coherent interface across the full range of dopant stoichiometries considered. Increasing x_{Li} increases the degree of lattice mismatch with respect to both candidate electrodes. At high mismatch values it becomes increasingly likely that dislocations or other extended defects form, which relieve the interfacial strain, and which may have additional effects on lithium transport. In practice, high quality interfaces may require thin films of electrolyte, which are more able to preserve epitaxy under large lattice misfits [27].

We find that in (Li,Al)-co-doped spinel, isotropic tensile strain reduces lithium diffusion barriers, from ~ 0.4 eV to ~ 0.2 eV under strains of up to 6%. This effect is correlated with changes in the volume of the octahedral site at the midpoint of each diffusion pathway, and

¹ The lattice parameters of $\text{Li}_y\text{Mn}_2\text{O}_4$ grow and shrink with lithium insertion and extraction, varying between 8.22 Å and 8.04 Å at $x_{\text{Li}} = 0.50$ and $x_{\text{Li}} = 0.14$ respectively [10]. $\text{Li}_{4+3z}\text{Ti}_5\text{O}_{12}$ is a “zero-strain material” whose lattice-parameters change by $< 0.1\%$ upon Li intercalation and extraction [11–13].

² Interestingly, the local DFT-NEB diffusion barriers for lithium motion calculated by Mees *et al.* [25] are broadly independent of dopant concentration, suggesting that the dominant effect of stoichiometry on the lithium diffusion coefficient is due to changes in the connectivity of available diffusion pathways.

differences in diffusion barriers are approximately correlated with differences in electrostatic potential along specific paths. For anisotropic strain, which approximates an ideal coherent electrolyte–electrode interface, the transition site volume changes are much smaller, and the corresponding effect on the lithium-diffusion barrier height is weaker. These results indicate that isotropic strain is expected to have a large impact on ionic conductivities in (Li,Al)–co-doped spinel electrolytes, with tensile strain being a potential route to enhanced lithium transport. For “lattice-matched” electrolyte–electrode systems, however, providing interfaces remain coherent, the residual epitaxial strain is not expected to strongly affect lithium transport.

METHODS

All calculations were performed using the plane-wave DFT code VASP [28, 29]. Exchange and correlation effects were approximated by the revised Perdew-Burke-Ernzerhof generalized gradient approximation (GGA) PBEsol functional [30]. The pseudopotential method was used in the form of projector augmented wave (PAW) pseudopotentials to treat core electrons [31] with 3 valence electrons for Al ($3s^23p^1$), 1 valence electron for Li ($2s^1$), 6 valence electrons for O ($2s^22p^6$), and 2 valence electrons for Mg ($3s^2$). All calculations were performed on 56 atom cells, and k -space sampling was performed on a $(3 \times 3 \times 3)$ Monkhorst-Pack grid. The plane-wave cut-off energy was 600 eV for calculations with variable cell shape and volume, and 550 eV for calculations with fixed cell shape. Geometry optimisations, including the CI-NEB calculations were, were deemed converged when the forces on ions were less than 1×10^{-2} eV \AA^{-1} .

The conventional spinel structure belongs to the $Fd\bar{3}m$ spacegroup, and has 56 ions in the unit cell, with stoichiometry $(A^{2+})[B_2^{3+}]O_4$. In the normal magnesium-spinel structure, $(Mg)[Al_2]O_4$, Mg^{2+} cations occupy the tetrahedral 8a Wyckoff positions, Al^{3+} cations occupy the octahedral 16d Wyckoff positions, and O^{2-} anions occupy the 32e positions [32, 33]. Upon co-doping with $\{Li, Al\}$, pairs of Mg^{2+} cations are substituted in equal proportion by Li^+ and Al^{3+} , to maintain charge neutrality, giving a composition of $(Al_xMg_{1-2x}Li_x)[Al_2]O_4$ [6, 25]. The maximum possible dopant content is $x_{Li} = 0.5$ (Fig. 1).

For our calculations, we consider dopant concentrations of $x_{Li} = 0.25$ and $x_{Li} = 0.5$. Substitutional doping at the Mg sites lowers the crystal symmetry, making the A-site cations non-equivalent. To account for this A-site disorder we identified all symmetry inequivalent structures at each dopant concentration using the `bsym` code [34]. In a 56 atom cell, this gives 7 structures at $x_{Li} = 0.25$ and 4 structures at $x_{Li} = 0.5$. Fig. 1 shows examples of these doped structures alongside the undoped magnesium-spinel structure. Li^+ diffusion between the

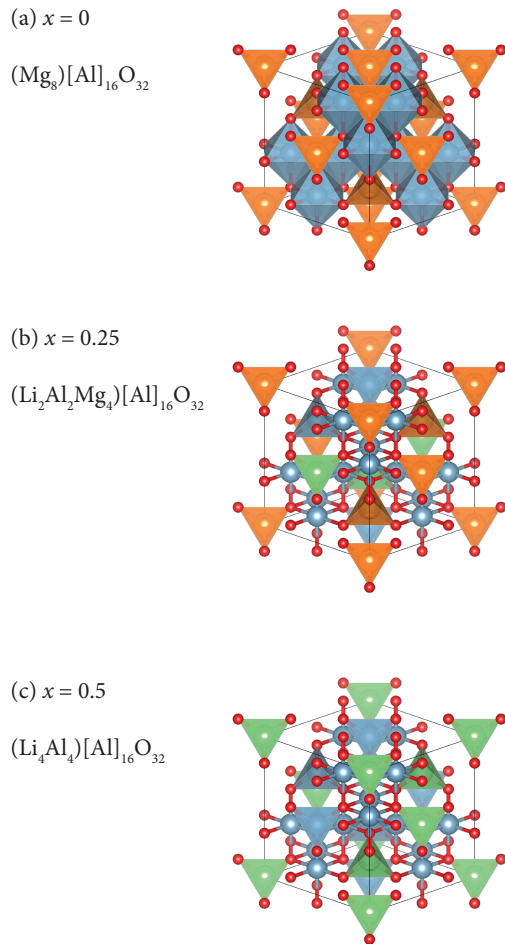


FIG. 1. Example 56 atom unit cells for undoped and (Li,Al)-doped spinel structures with composition $(Al_xMg_{1-2x}Li_x)[Al_2]O_4$. (a) The undoped parent spinel ($x_{Li} = 0$): $(Mg_8)[Al_{16}]O_{32}$, (b) 50% doped ($x_{Li} = 0.25$): $(Al_2Li_2Mg_4)[Al_{16}]O_{32}$, (c) Fully doped ($x_{Li} = 0.5$): $(Al_4Li_4)[Al_{16}]O_{32}$. Mg atoms are orange, Al atoms are blue, Li atoms are green, and O atoms are red.

tetrahedral A-sites proceeds via 8a–16c–8a paths, with the vacant 16c octahedra connecting the end-point tetrahedra (Fig. 2).

In this study we focus on vacancy-mediated lithium-ion transport, following the approach of Mees *et al.* [25]. For each inequivalent doped structure, we generated the full set of possible lithium-diffusion pathways by removing, in turn, each of the A-site lithium ions. At a dopant content of $x_{Li} = 0.25$, three of the seven initial symmetry inequivalent structures have viable lithium diffusion pathways, where a lithium ion can move from an occupied A site, through an octahedral 16c site, into a previously unoccupied destination A-site. These three structures have one unique pathway each, which can be traversed in either direction. At a dopant content of $x_{Li} = 0.5$, three of the four symmetry inequivalent structures have viable lithium-diffusion pathways. Two of these struc-

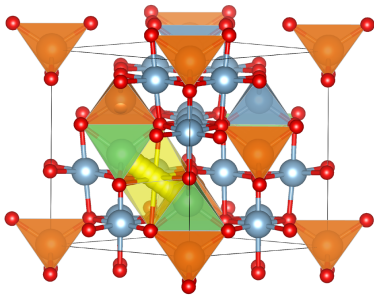


FIG. 2. Li^+ diffusion pathway between neighbouring A cation sites via the 16c octahedral vacancy (yellow).

tures have a single pathway, and the third structure has two. To sample these different diffusion pathways, we consider all three inequivalent paths at $x_{\text{Li}} = 0.25$, and three of the available paths at $x_{\text{Li}} = 0.5$. For each candidate pathway, we have performed a series of CI-NEB calculation to evaluate the potential energy profile of a diffusing lithium ion [26]. We denote specific pathways using S_x^p , where S describes the target strain (U = unstrained, LM = lithium manganate lattice parameters, LT = lithium titanate lattice parameters), x is the dopant concentration x_{Li} , and p enumerates the pathways. An additional superscript R indicates a “reversed” pathway in cases where the diffusion profile is not symmetric.

The different strain protocols; unstrained, isotropic, and epitaxial; are illustrated schematically in Fig. 3. In all cases, we consider strains corresponding to model $\{100\}_A\{100\}_B$ coherent interfaces between the doped (Mg,Al)-spinel and the target electrode (lithium manganate or lithium titanate spinel). To model isotropic strain, all three lattice parameters are equally scaled to match that of the target electrode. For anisotropic epitaxial strain, only two of the lattice parameters are adjusted to match the target lattice. The perpendicular lattice parameter is relaxed to minimise the total cell energy.

In addition to potential energy profiles from our CI-NEB calculations, we also present electrostatic potential profiles along each path. These are defined as the average electrostatic potential at the site of the mobile ion, evaluated at the optimised geometry of each NEB image. If a diffusing lithium ion is approximated as a +1 point charge, then the potential energy surface is characterised entirely by the electrostatic interactions between the mobile lithium ion and the surrounding lattice. Previous computational studies of lithium-ion diffusion in electrodes have shown that electrostatic potential profiles often give a good approximate description of diffusion barrier profiles [35–37]. In real systems, however, the interactions between mobile lithium ions and the host lattice are not purely electrostatic. Lithium ions also experience short-ranged repulsion from nearby lattice ions, due to overlapping valence electron densities.

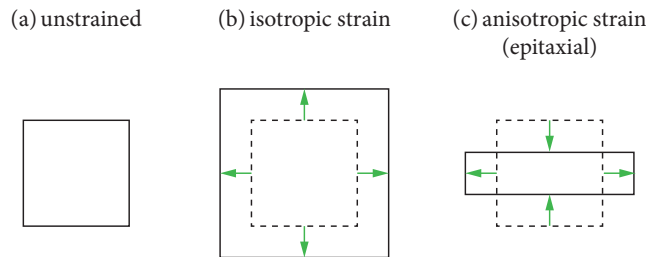


FIG. 3. 2D schematic illustrating the unstrained, isotropically strained, and anisotropically strained calculations. (a) Unstrained: all lattice parameters are relaxed during the DFT calculation ($a, b, c = a^{\text{DFT}}$) (b) Isotropic strain: all three lattice parameters are scaled to match those of the target electrode ($V_{\text{Cell}} = V_{\text{electrode}}$) (c) Anisotropic strain: the two in-plane lattice parameters are scaled to match those of the target electrode, and the perpendicular lattice parameter is relaxed ($[a, b = a^{\text{electrode}}, c = c^{\text{DFT}}]$, $[b, c = a^{\text{electrode}}, a = a^{\text{DFT}}]$, $[a, c = a^{\text{electrode}}, b = b^{\text{DFT}}]$)

The detailed shape of a diffusion potential energy profile therefore depends on the balance of the electrostatic and short-ranged repulsive interactions.³ In general, short-ranged repulsion is expected to be reduced under expansive strain. Our inclusion of electrostatic potential energy profiles is motivated, in part, by an interest in the extent to which this conceptually simple metric describes lithium-ion diffusion in (Li,Al)-co-doped spinel electrolytes [36, 37].

To better understand the role of A-site cation disorder on lithium diffusion profiles, we also parameterise how the A-site coordination environments differ from those in undoped MgAl_2O_4 . We have followed the analysis of Mees *et al.*, who noted that the energy of different co-doped spinel structures is correlated with the “average” local oxidation state for the A-site cations, μ_i [25]. For a specific A-site, μ_i is defined as the average formal oxidation state; $O_{\text{Li}} = +1$, $O_{\text{Mg}} = +2$, $O_{\text{Al}} = +3$, $O_{\text{vacancy}} = 0$; of the ions occupying the central A-site, and the four nearest-neighbour A-sites:

$$\mu_i = \frac{1}{5} \left(O_i + \sum_{j \in \{\text{nn}_i^A\}} O_j \right) \quad (1)$$

Structures with lower energies tend to have average μ values closer to +2, i.e. the value obtained for A-site Mg ions in the undoped parent structure. Deviations from this “optimal” average nearest-neighbour oxidation state can be quantified by calculating the root-mean-square

³ For the sake of this conceptual analysis, we neglect lithium ion polarisation and dispersion interactions. Both contributions are expected to be small, due to the compact $1s^2$ electron configuration of Li^+ .

difference between μ_i and the optimal value of +2 for all occupied A-sites in each structure:

$$\sigma_A = \sqrt{\frac{\sum_i (\mu_i - 2)^2}{7}}. \quad (2)$$

Inputs and outputs for our VASP calculations are openly available under the CC-BY-SA-4.0 license [38]. This dataset includes Python scripts for extracting the NEB profiles and electrostatic potential profiles from the DFT calculation outputs, and code for calculating σ_A (Eqn. 2). Analysis codes that produce Figs. 4–8 are available as a Jupyter notebook [39], published under the MIT license. Figs. 1 and 2 were generated using VESTA [40].

RESULTS

Unstrained (Li,Al)–co-doped spinel

We first consider lithium diffusion pathways in unstrained (Li,Al)–co-doped spinel, $(\text{Al}_x\text{Mg}_{1-2x}\text{Li}_x)[\text{Al}_2]\text{O}_4$, using DFT-optimised lattice parameters for each dopant concentration. The potential energy profiles for the minimum-energy pathways for lithium diffusion are shown in Fig. 4. The energy barriers for diffusion between adjacent A-sites are in the range ~ 0.30 – 0.45 eV. These energies are consistent with those from the previous DFT NEB study of Mees *et al.* [25], and with values from NMR analysis of lithium jumps between lattice sites in these materials [6].

(Li,Al)-codoping of MgAl_2O_4 introduces disorder across the A-sites, and makes the lithium-occupied A-sites non-equivalent. From the perspective of a cation occupying a particular A-site, the local effect of this disorder is to introduce variation into the nearest-neighbour A-site occupation: each neighbouring A-site may now contain Li, Mg, or Al, or be vacant. For each lithium diffusion pathway, the nearest-neighbour A-site occupations for the end-point configurations allows classification into “symmetric” or “asymmetric” paths. Pathways with identical nearest-neighbour A-site coordination environments at both end-points are symmetric, while those with different coordination environments are asymmetric.

For the symmetric pathways, the diffusion barrier is necessarily equal moving in in both directions. For asymmetric pathways, however, the end-point energies may differ, and the potential energy profile relative to the starting structure depends on the direction of lithium diffusion. For the asymmetric pathways considered here, we present data for lithium diffusion in both forward and reverse directions, with the latter indicated with a superscript R.

The relative energies of the two endpoints for an asymmetric path can be analysed in terms of σ_A (Eqn. 2),

which describes the average A-site oxidation-state deviation from that of MgAl_2O_4 . For the $\text{U}_{0.25}^3$ path, the lower energy end-point gives 0.1069, and the higher energy end-point gives 0.3207. Similarly, for the $\text{U}_{0.50}^3$ path, the lower energy end-point gives 0.2000, and the higher energy end-point gives 0.4721. In both cases, the lower energy end-point gives the lower value of σ_A , indicating a more uniform arrangement of formal charges on the spinel lattice.

The electrostatic potential profiles approximately follow the potential energy profiles. For each path, the calculated electrostatic potential barrier typically overestimates the NEB barrier. This is consistent with lithium ions experiencing stronger short-ranged repulsion at the tetrahedral A sites than at the intermediate octahedral sites. This increases the energies of lithium at each end-point relative to the NEB path maximum. For the $\text{U}_{0.5}^3$ (and $\text{U}_{0.5}^{3R}$) paths, there is quantitative disagreement between the electrostatic potential profile and the NEB potential profile. The electrostatic potential predicts the incorrect energy ordering of the two end-points. This illustrates that the electrostatic potential alone is not guaranteed to give a good description of the potential energy surface for mobile lithium ions.

Isotropically-strained (Li,Al)–co-doped spinel

We now consider the effect of isotropic strain on diffusion. We have calculated NEB barriers for both dopant concentrations with the unit cell strained to the $\text{Li}_y\text{Mn}_2\text{O}_4$ and $\text{Li}_{4+3z}\text{Ti}_5\text{O}_{12}$ lattice volumes (Fig. 4). Isotropic strain has a large impact on the diffusion barriers. For the symmetric pathways the effect of this strain is straightforward: increased tensile strain decreases the diffusion barriers at both dopant concentrations. This result mirrors the effects seen in many solid oxide fuel cell electrolytes [16–18, 20], where tensile strain typically increases oxide ion diffusion.

For the asymmetric pathway the situation is more complicated. Because asymmetric paths necessarily have inequivalent endpoints, the applied strain can affect their *relative* energies. The change in the diffusion barrier height therefore depends on the direction of motion along the path. At $x_{\text{Li}} = 0.25$ the barrier is reduced for the forward pathway (3), but slightly increases for the reverse path (3R). At $x_{\text{Li}} = 0.5$ this asymmetry is even more pronounced, with a large barrier increase for the forward path (3), but a large decrease for the reverse path (3R). Fig. 5 plots the relative change in volume for the intermediate octahedral site against the change in barrier height. For both $x_{\text{Li}} = 0.25$ and $x_{\text{Li}} = 0.50$, the average trend of decreasing the NEB barrier height is apparent. The outliers (showing both increased and strongly decreased barrier heights) correspond to the two asymmetric paths described above.

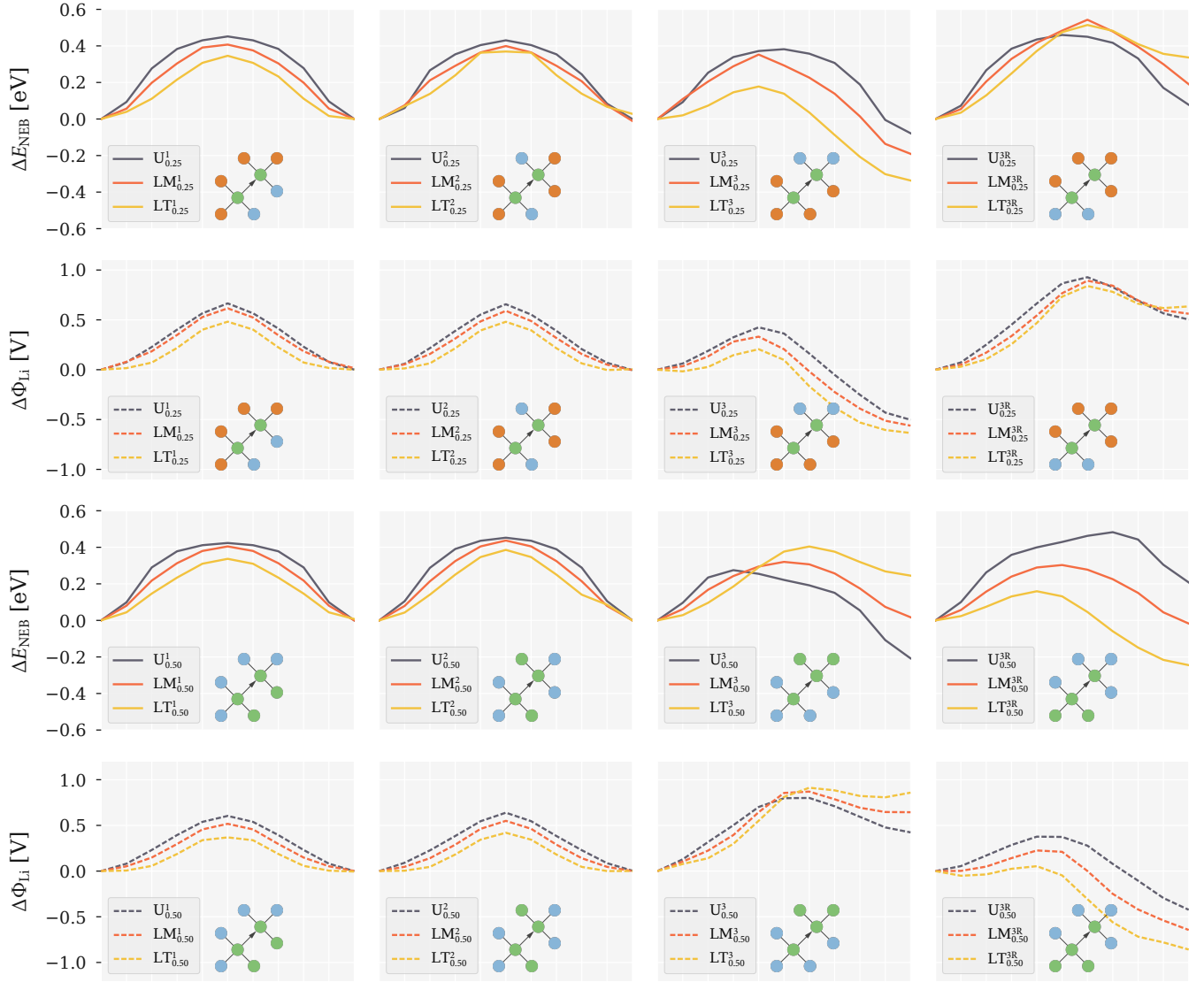


FIG. 4. cNEB energy profiles and corresponding electrostatic potential profiles for unstrained and isotropically strained structures ($x_{\text{Li}} = 0.25$ (top) and $x_{\text{Li}} = 0.5$ (bottom)). Notation is as follows: S_x^p , where S is strain (U = unstrained, LM = strained to lithium manganate lattice parameters, LT = strained to lithium titanate lattice parameters), x is the dopant concentration and p enumerates the pathways (where R refers to the same pathway in reverse). The inset schematic in each panel shows the coordination environments of the initial and final A-site positions. Li ions are green, Mg are orange and Al are blue. Electrostatic potential profiles (including the contribution from the mobile Li^+ ion) at the Li^+ site along the diffusion pathway are shown by the corresponding coloured dashed lines.

The effect of strain on the NEB profiles is mirrored by the electrostatic potential profiles, suggesting that changes in electrostatic potential do provide at least a qualitative metric for predicting the effects of strain on lithium ion diffusion. Fig. 6 plots the NEB barrier against the electrostatic barrier for each path. Linear-least-squares fits for each strain protocol show that the electrostatic potential barrier becomes an increasingly good predictor of the NEB barrier at larger strains. This is consistent with short-ranged repulsion interactions being less significant as the lattice volume increases under ten-

sile strain.

The effect of isotropic strain on the asymmetric paths can also be examined from the perspective of the σ_{A} values for each end-point. For both asymmetric paths, $S_{0.25}^3$ and $S_{0.50}^3$, tensile strain produces a relative stabilisation of the end-point structure that more strongly deviates from the average +II oxidation state of the parent MgAl_2O_4 spinel, i.e. the structure with the larger σ_{A} . At $x_{\text{Li}} = 0.5$, this effect is large enough that the relative stabilities of the two end-points are reversed, contradicting the general trend that higher σ values correspond to less

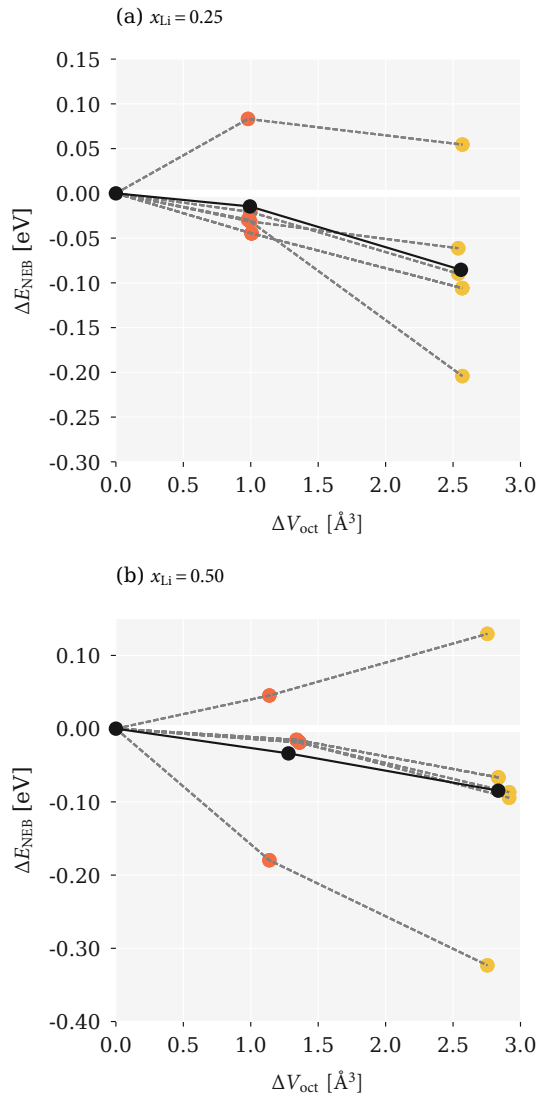


FIG. 5. Isotropic strain induced ΔE in the NEB barrier height versus the 16c polyhedra volume change for (a) $x_{\text{Li}} = 0.25$ (b) $x_{\text{Li}} = 0.50$. Red and orange circles correspond to strain to $\text{Li}_y\text{Mn}_2\text{O}_4$ and $\text{Li}_{4+3z}\text{Ti}_5\text{O}_{12}$ lattice parameters, respectively. Dashed lines link equivalent pathways under different strains. The solid black points show mean values under each strain condition.

stable structures.

Anisotropically-strained (Li,Al)-co-doped spinel

In the previous section, we have explored the effect of isotropic strain on lithium-ion diffusion. For a hypothetical lattice-matched electrolyte–electrode interface, however, lattice strain due to electrolyte–electrode epitaxy is not isotropic, but instead is anisotropic. Specifically, the lattice will be strained parallel to the interface, but is free to relax in the perpendicular direction.

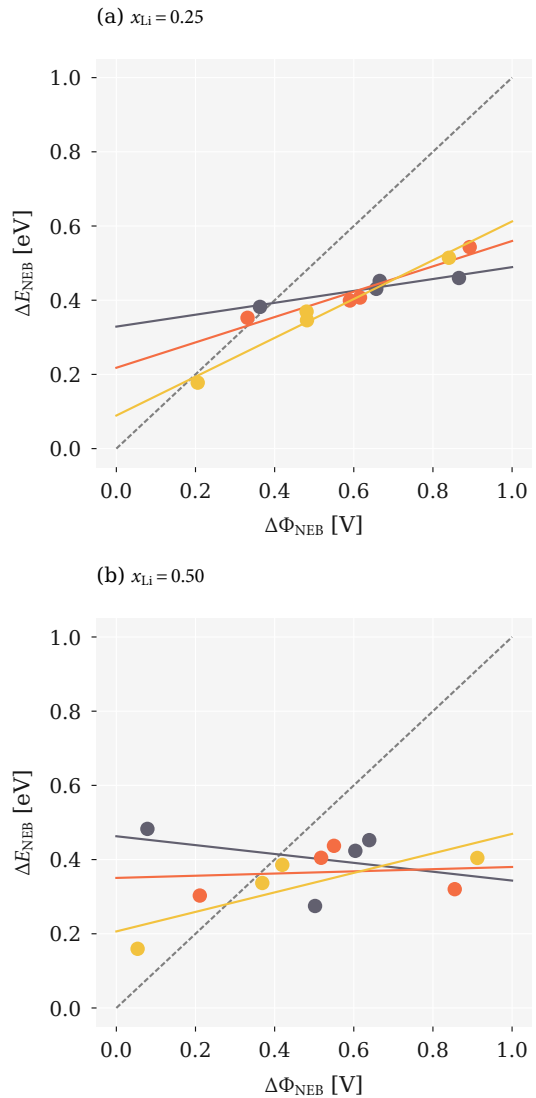


FIG. 6. Electrostatic potential barrier, $\Delta\Phi_{\text{NEB}}$, versus potential energy barrier, ΔE_{NEB} , for the diffusing lithium ion, for pathways under zero-strain (black), and isotropically strained to the $\text{Li}_y\text{Mn}_2\text{O}_4$ (red) and $\text{Li}_{4+3z}\text{Ti}_5\text{O}_{12}$ (orange) cell volumes. (a) $x_{\text{Li}} = 0.25$. (b) $x_{\text{Li}} = 0.50$. The solid lines show linear best fits at each strain (U, LM, LT). The diagonal dashed line corresponds to an exact 1:1 relationship between $\Delta\Phi_{\text{NEB}}$ and ΔE_{NEB} .

To model the strain at a hypothetical lattice-matched electrolyte–electrode interface, we therefore extended our calculations on isotropically strained systems to consider the effect of anisotropic strain on the CI-NEB diffusion pathways. For these calculations, we still consider strain as arising from coherent $\{100\}_{\text{A}}|\{100\}_{\text{B}}$ heterointerfaces. Under anisotropic strain, the three $\{100\}$ directions become inequivalent, and we consider each possible strain orientation. For each calculation, the two in-plane lattice parameters are strained to match experimental values of either $\text{Li}_y\text{Mn}_2\text{O}_4$ or $\text{Li}_{4+3z}\text{Ti}_5\text{O}_{12}$, and the third lattice

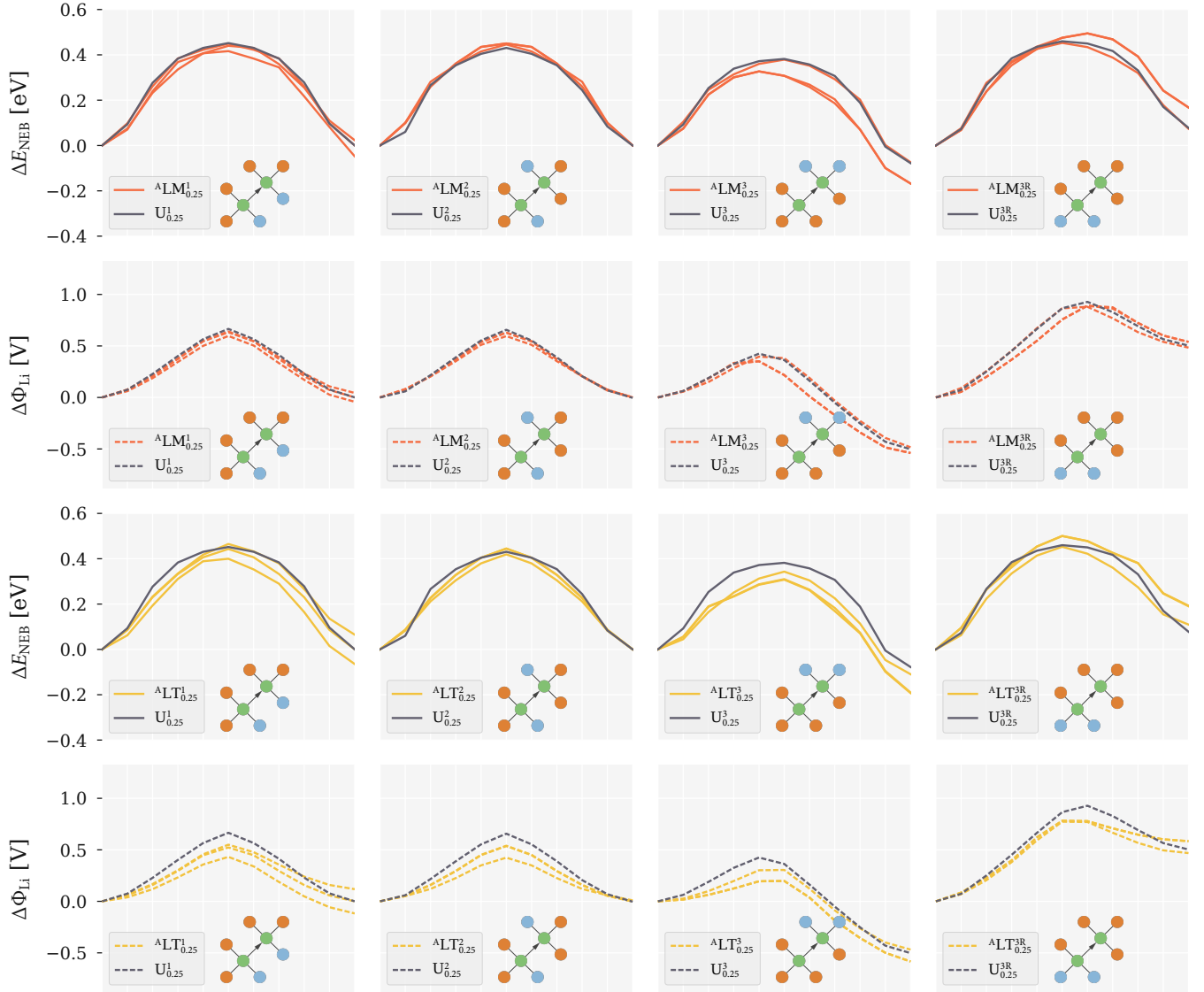


FIG. 7. cNEB energy profiles and corresponding electrostatic potential profiles for unstrained and anisotropically strained structures ($x_{\text{Li}} = 0.25$ (top) and $x_{\text{Li}} = 0.5$ (bottom)). Notation is as follows: S_x^p , where S is strain (U = unstrained, LM = strained to lithium manganate lattice parameters, LT = strained to lithium titanate lattice parameters), x is the dopant concentration and p enumerates the pathways (where R refers to the same pathway in reverse). A superscript A indicates anisotropic strain along only two axes. The inset schematic in each panel shows the coordination environments of the initial and final A -site positions. Li ions are green, Mg are orange and Al are blue. Electrostatic potential profiles (including the contribution from the mobile Li^+ ion) at the Li^+ site along the diffusion pathway are shown by the corresponding coloured dashed lines.

parameter is optimised to minimise the total system energy. Because we consider only $\{100\}$ oriented interfaces, this is equivalent to biaxial strain.

The effect of anisotropic strain on diffusion barrier height is much smaller than in the isotropic case, with typical changes of the order of 0.01–0.1 eV. Individual quantitative changes are sensitive to the exact path being considered, and to the orientation of the applied strain (Fig. 7). The NEB pathway again depends on the symmetry of the start- and end-point A cation sites. In some

cases, however, the application of planar strain breaks the symmetry found in the isotropic and unstrained structures. This point is illustrated by the $^A\text{LM}_{0.25}^1$ and $^A\text{LT}_{0.25}^1$ pathways (Fig. 7) where the energy difference between the start- and end-points depends on the orientation of the applied strain.

For the symmetric isotropically strained pathways, discussed above, the effect on the electrostatic potential under strain gave a good indication of the effect on the NEB diffusion barrier. This simple electrostatic model is

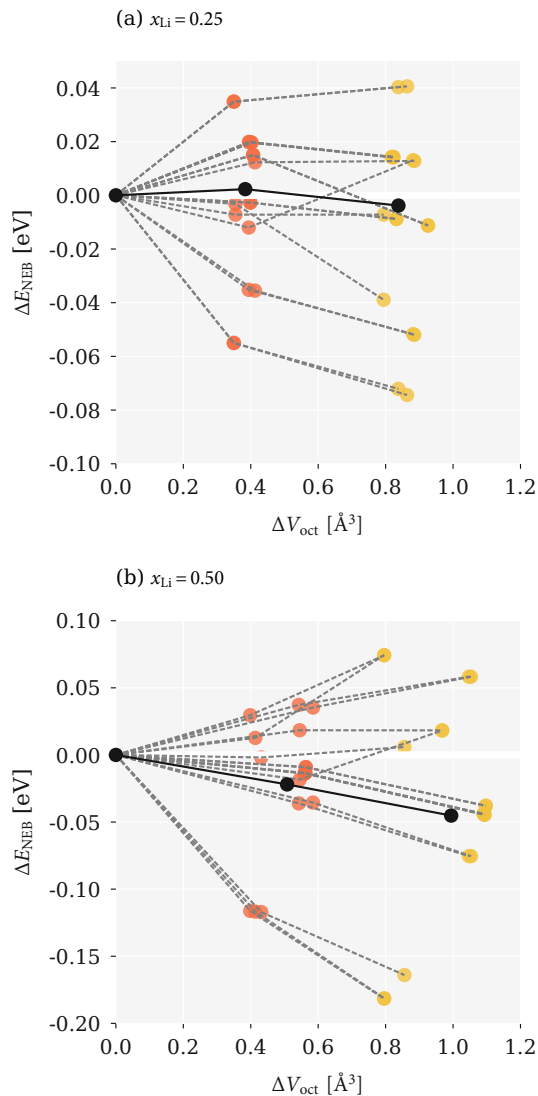


FIG. 8. Anisotropic strain induced ΔE in the NEB barrier height versus the 16c polyhedra volume change for (a) $x_{\text{Li}} = 0.25$ (b) $x_{\text{Li}} = 0.5$. Red and orange circles show strain to $\text{Li}_y\text{Mn}_2\text{O}_4$ and $\text{Li}_{4+3z}\text{Ti}_5\text{O}_{12}$ lattice parameters, respectively. Dashed lines link equivalent pathways under different strains. The solid black points show mean values under each strain condition.

not applicable, however, for the antisymmetric pathways. Under anisotropic strain, we find that the effect on the electrostatic potential is no longer a useful predictor of the change in NEB barrier: in some cases the electrostatic potential barrier decreases while the NEB barrier increases. The electrostatic potential profiles also show the effect of the applied strain lowering the cell symmetry, with relative potentials of path end-points now varying with the orientation of the applied strain (see ${}^{\text{A}}\text{LM}_{0.25}^1$, ${}^{\text{A}}\text{LT}_{0.25}^1$, ${}^{\text{A}}\text{LM}_{0.25}^3$, ${}^{\text{A}}\text{LT}_{0.25}^3$, ${}^{\text{A}}\text{LM}_{0.25}^{3\text{R}}$, and ${}^{\text{A}}\text{LT}_{0.25}^{3\text{R}}$ in Fig. 7). For isotropic strain, we observed a direct relationship between the volume of the transitional octahedral 16c

site, and the electrostatic potential at the diffusing Li^+ site. For these anisotropically strained calculations, we find that the octahedral site volume changes are much smaller than those due to the equivalent isotropic strain, because the cell is allowed to contract along the free axis. As a result of this reduced volume change, the general effect on diffusion barriers typically is much smaller than that of the isotropically strained equivalents (Figs. 7 & 8).

SUMMARY & DISCUSSION

(Li,Al)-codoped MgAl_2O_4 represents a new class of spinel-structured lithium-ion solid electrolytes, with potential applications in an all-spinel solid-state lithium-ion battery [6], or as an electrode–buffer-layer [41], with lattice-matched electrolyte–electrode interfaces. Any lattice-matched (or epitaxial) interface between an electrode and electrolyte will exhibit some residual intrinsic strain. In the case of (Li,Al)-codoped MgAl_2O_4 , hypothetical lattice-matched (100) interfaces with the spinel electrodes $\text{Li}_y\text{Mn}_2\text{O}_4$ or $\text{Li}_{4+3z}\text{Ti}_5\text{O}_{12}$ require tensile strains of 3.2 or 6.0% respectively. Because the lattice parameter of (Li,Al)-codoped MgAl_2O_4 decreases with higher doping levels, it has previously been suggested that high dopant concentrations ($x_{\text{Li}} > 0.3$) should be avoided, to minimise possible corresponding increases in interfacial resistance [25]. High dopant concentrations, however, have been predicted to have higher lithium conductivities, making them more appealing as solid electrolytes. These issues have prompted us to conduct this computational study into the effects of tensile strain on the lithium-ion diffusion pathways in (Li,Al)-doped MgAl_2O_4 , to assess the extent to which the increased strain expected at higher dopant concentrations affects lithium-ion transport.

We have performed a series of climbing-image nudged-elastic-band (CI-NEB) calculations to evaluate the potential energy profile for lithium vacancy diffusion, which proceeds via tetrahedron–octahedron–tetrahedron paths through the spinel structure. Our calculations show that isotropic strain, in most cases, decreases diffusion barriers; typically by ~ 0.1 eV for a lattice strained to match $\text{Li}_{4+3z}\text{Ti}_5\text{O}_{12}$. This decrease is correlated with changes in the electrostatic potential profile along each diffusion path. The electrostatic potential profile, however, does not give a good prediction of potential energy barriers for all paths, particularly in cases where paths are asymmetric. As the lattice volume increases under tensile strain, however, we find that the electrostatic potential profile becomes an increasingly good proxy for the diffusion potential energy profile.

For a realistic lattice-matched interface, the resulting strain will be anisotropic (epitaxial). From our CI-NEB calculations of anisotropically strained cells, we predict a

much smaller change in diffusion barriers than for equivalent isotropic strain. The effect of anisotropic tensile strain is still, typically, to decrease lithium-ion diffusion barriers, particularly at higher dopant concentrations; with changes in barrier height of the order of 0.01–0.1 eV. There is a large variance in the barrier height changes; some barriers increase under epitaxial tensile strain. The quantitative details depend on the specific path under consideration, and on the relative orientation of the applied strain. From an “average” perspective, then, epitaxial strain at a lattice-matched interface is not expected to significantly change local diffusion barriers, and is therefore not expected to increase interfacial resistance by changing local ion-hopping rates. Precisely quantifying the effect of strain on ensemble transport properties (diffusion coefficients and ionic conductivities), however requires statistical sampling of all relevant paths, for example, using molecular dynamics or kinetic Monte Carlo simulations (cf. ref. [25]).

Changes to local diffusion barriers are not the only possible mechanism by which interfacial strain might affect interfacial resistance. At a heterointerface between an electrode and electrolyte, the standard chemical potential of lithium ions may differ between the two materials. This can drive a spontaneous redistribution of the mobile ions across the interface to form space-charge layers on each side [42]. The change in local lithium-ion concentration associated with space-charge formation can affect the local conductivity (and resistivity) either positively or negatively, and hence contributes to interfacial resistance. Because strain shifts the local electrostatic potential, interfacial strain changes the standard electrochemical potential offset at an electrolyte–electrode interface. This consequently affects space-charge formation, and the associated space-charge contribution to interfacial resistance. Our study also implicitly assumes that any relevant epitaxial heterointerface between electrode and electrolyte can be formed without dislocations or other extended defects. Both these issues should be considered when evaluating the potential of lattice-matched electrolyte–electrode interfaces for engineering low-interfacial resistance cells. Our results, however, indicate that strain effects on local diffusion barriers are likely not a factor in assessing candidate electrolyte–electrode lattice-matched pairings.

DATA ACCESS STATEMENT

The DFT dataset supporting this study is available from the University of Bath Research Data Archive (doi: 10.15125/BATH-00438) [38], published under the CC-BY-SA-4.0 license. This dataset contains input parameters and output files for all VASP calculations, and a series of Python scripts for collating relevant data from the VASP outputs. A Jupyter notebook contain-

ing code to produce Figs. 4–8 is also available (Ref 39, doi: 10.5281/zenodo.1069417), published under the MIT license.

ACKNOWLEDGEMENTS

This work was funded by EPSRC grant EP/N004302/1. B. J. M. acknowledges support from the Royal Society (UF130329). Calculations were performed using the Balena High Performance Computing Service at the University of Bath, and using the ARCHER supercomputer, with access through membership of the UK’s HPC Materials Chemistry Consortium, funded by EPSRC grant EP/L000202.

* c.o.rourke@bath.ac.uk

† b.j.morgan@bath.ac.uk

- [1] P. Knauth, *Sol. Stat. Ionics* **180**, 911 (2009).
- [2] J. C. Bachman, S. Muy, A. Grimaud, H.-H. Chang, N. Pour, S. F. Lux, O. Paschos, F. Maglia, S. Lupart, P. Lamp, L. Giordano, and Y. Shao-Horn, *Chem. Rev.* **116**, 140 (2016).
- [3] A. Manthiram, X. Yu, and S. Wang, *Nat. Rev. Mater.* **2**, 1 (2017).
- [4] N. Kamaya, K. Homma, Y. Yamakawa, M. Hirayama, R. Kanno, M. Yonemura, T. Kamiyama, Y. Kato, S. Hama, K. Kawamoto, and A. Mitsui, *Nat. Mater.* **10**, 682 (2011).
- [5] D. Santhanagopalan, D. Qian, T. McGilvray, Z. Wang, F. Wang, F. Camino, J. Graetz, N. Dudney, and Y. S. Meng, *J. Phys. Chem. Lett.* **5**, 298 (2014).
- [6] F. Rosciano, P. P. Pescarmona, K. Houthoofd, A. Persoons, P. Bottke, and M. Wilkening, *Phys. Chem. Chem. Phys.* **15**, 6107 (2013).
- [7] M. M. Thackeray and J. B. Goodenough, “Solid state cell wherein an anode, solid electrolyte and cathode each comprise a cubic-close-packed framework structure,” (1985), US Patent 4,507,371.
- [8] E. S. M. Blaakmeer, F. Rosciano, and E. R. H. van Eck, *J. Phys. Chem. C* **119**, 7565 (2015).
- [9] R. Djenadic, M. Botros, and H. Hahn, *Sol. Stat. Ionics* **287**, 71 (2016).
- [10] H. Berg and J. O. Thomas, *Sol. Stat. Ionics* **126**, 227 (1999).
- [11] M. Wagemaker, D. Simon, E. Kelder, J. Schoonman, C. Ringpfeil, U. Haake, D. Lützenkirchen-Hecht, R. Frahm, and F. Mulder, *Adv. Mater.* **18**, 3169 (2006).
- [12] F. Ronci, P. Reale, B. Scrosati, S. Panero, V. Rossi Albertini, P. Perfetti, M. di Michiel, and J. M. Merino, *J.*

- Phys. Chem. B **106**, 3082 (2002).
- [13] B. J. Morgan, J. Carrasco, and G. Teobaldi, *J. Mater. Chem. A* **4**, 17180 (2016).
- [14] N. Schichtel, C. Korte, D. Hesse, and J. Janek, *Phys. Chem. Chem. Phys.* **11**, 3043 (2009).
- [15] J. L. M. Rupp, *Sol. Stat. Ionics* **207**, 1 (2012).
- [16] K. Wen, W. Lv, and W. He, *J. Mater. Chem. A* **3**, 20031 (2015).
- [17] B. Yildiz, *MRS Bull.* **39**, 147 (2014).
- [18] H. Aydin, C. Korte, M. Rohnke, and J. Janek, *Phys. Chem. Chem. Phys.* **15**, 1944 (2013).
- [19] W. Shen, J. Jiang, and J. L. Hertz, *RSC Adv.* **4**, 21625 (2014).
- [20] A. Fluri, D. Pergolesi, V. Roddatis, A. Wokaun, and T. Lippert, *Nat. Comm.* **7** (2016), 10.1038/ncomms10692.
- [21] F. Ning, S. Li, B. Xu, and C. Ouyang, *Sol. Stat. Ionics* **263**, 46 (2014).
- [22] J. Wei, D. Ogawa, T. Fukumura, Y. Hirose, and T. Hasegawa, *Crys. Growth & Design* **15**, 2187 (2015).
- [23] C. Tealdi, J. Heath, and M. S. Islam, *J. Mater. Chem. A* **4**, 6998 (2016).
- [24] A. Moradabadi, P. Kaghazchi, J. Rohrer, and K. Albe, *arXiv* (2017), 1706.01709v1.
- [25] M. J. Mees, G. Pourtois, F. Rosciano, B. Put, P. M. Vereecken, and A. Stesmans, *Phys. Chem. Chem. Phys.* **16**, 5399 (2014).
- [26] G. Henkelman, B. P. Uberuaga, and H. Jónsson, *J. Chem. Phys.* **113**, 9901 (2000).
- [27] B. S. Allimi, M. Aindow, and S. P. Alpay, *Appl. Phys. Lett.* **93**, 112109 (2008).
- [28] G. Kresse and J. Furthmüller, *Phys. Rev. B* **54**, 11169 (1996).
- [29] G. Kresse and J. Furthmüller, *Comp. Mater. Sci.* **6**, 15 (1996).
- [30] J. P. Perdew, A. Ruzsinszky, G. I. Csonka, O. A. Vydrov, G. E. Scuseria, L. A. Constantin, X. Zhou, and K. Burke, *Phys. Rev. Lett.* **100**, 136406 (2008).
- [31] P. E. Blöchl, *Phys. Rev. B* **50**, 17953 (1994).
- [32] K. E. Sickafus, J. M. Wills, and N. W. Grimes, *J. Am. Ceram. Soc.* **82**, 3279 (1999).
- [33] R. J. Hill, J. R. Craig, and G. V. Gibbs, *Phys. Chem. Mater.* **4**, 317 (1979).
- [34] B. J. Morgan, *The Journal of Open Source Software* **2** (2017), 10.21105/joss.00370.
- [35] B. J. Morgan and G. W. Watson, *Phys. Rev. B* **82**, 144119 (2010).
- [36] D. A. Tompsett, S. C. Parker, P. G. Bruce, and M. S. Islam, *Chem. Mater.* **25**, 536 (2013).
- [37] Z. Rong, D. Kitchaev, P. Canepa, W. Huang, and G. Ceder, *J. Chem. Phys.* **145**, 074112 (2016).
- [38] C. O'Rourke and B. J. Morgan, "DFT dataset for "Interfacial strain effects on lithium diffusion pathways in the spinel solid electrolyte Li-doped MgAl_2O_4 ,"" <https://doi.org/10.15125/BATH-00438> (2017).
- [39] C. O'Rourke and B. J. Morgan, "Data analysis for "Interfacial strain effects on lithium diffusion pathways in the spinel solid electrolyte Li-doped MgAl_2O_4 ,"" https://github.com/bjmorgan/data_NEB_spinel (2017).
- [40] K. Momma and F. Izumi, *J. Appl. Cryst.* **44**, 1272 (2011).
- [41] B. Put, P. M. Vereecken, M. J. Mees, F. Rosciano, I. P. Radu, and A. Stesmans, *Phys. Chem. Chem. Phys.* **17**, 29045 (2015).
- [42] B. J. Morgan and P. A. Madden, *Phys. Rev. B* **89** (2014), 10.1103/PhysRevB.89.054304.